Research Article

VIE-FG-FFT for Analyzing EM Scattering from Inhomogeneous Nonmagnetic Dielectric Objects

Shu-Wen Chen, Hou-Xing Zhou, Wei Hong, and Jia-Ye Xie

State Key Laboratory of Millimeter Waves, Southeast University, Nanjing 210096, China

Correspondence should be addressed to Hou-Xing Zhou; hxzhou@emfield.org

A new realization of the volume integral equation (VIE) in combination with the fast Fourier transform (FFT) is established by fitting Green's function (FG) onto the nodes of a uniform Cartesian grid for analyzing EM scattering from inhomogeneous nonmagnetic dielectric objects. The accuracy of the proposed method is the same as that of the P-FFT and higher than that of the AIM and the IE-FFT especially when increasing the grid spacing size. Besides, the preprocessing time of the proposed method is obviously less than that of the P-FFT for inhomogeneous nonmagnetic dielectric objects. Numerical examples are provided to demonstrate the accuracy and efficiency of the proposed method.

1. Introduction

The volume integral equation (VIE) method [1] based on the method of moments (MoM) [2] is one of the efficient methods to analyze electromagnetic (EM) scattering from inhomogeneous dielectric objects. As is well known, for the traditional VIE-MoM, both the storage requirement and the computational complexity of a matrix-vector multiplication when an iterative method is applied are proportional to $O(N^2)$, where N denotes the number of unknowns. Therefore, the VIE-MoM is not suitable for the direct analysis of EM scattering from electrically large and inhomogeneous dielectric objects.

One of approaches for improving the efficiency of the VIE-MoM is the VIE in combination with the fast Fourier transform (FFT), and it already has several implementations, such as the VIE-AIM [3, 4], the VIE-P-FFT [5, 6], and the VIE-IE-FFT [7, 8], which are simply called the FFT-based methods. These implementations are all transplanted from the corresponding versions [9–12] for the surface integral equation (SIE) [13]. Not long ago, a new realization, the FG-FFT, of the SIE in combination with the FFT for the electric field integral equation (EFIE) was proposed [14] and soon extended to the combined field integral equation (CFIE) [15].

In this paper, the FG-FFT for the SIE will be extended to the VIE for analyzing EM scattering from inhomogeneous nonmagnetic dielectric objects, and resultant method is simply called the VIE-FG-FFT. The remainder of this paper is organized as follows. In Section 2, the VIE-FG-FFT is presented in detail. In Section 3, some numerical examples are provided to demonstrate the accuracy and efficiency of the VIE-FG-FFT. Finally, the conclusion is given in Section 4. In this paper, the time convention $e^{j\omega t}$ is assumed and suppressed.

2. Formulation

2.1. The Volume Integral Equation. The permittivity and permeability of the free space are denoted by ϵ_0 and μ_0, respectively. Let V denote the volumetric domain occupied by an inhomogeneous nonmagnetic dielectric object with relative permittivity ϵ_r and relative permeability $\mu_r = 1$ (meaning nonmagnetic).

Let $\vec{E}^i$ be the incident electric field and $\vec{E}^s$ the scattered electric field; then the total electric field $\vec{E}^{tot}$ can be expressed as the sum of $\vec{E}^i$ and $\vec{E}^s$:

$$\vec{E}^{tot} = \vec{E}^i + \vec{E}^s, \tag{1}$$

and the volume integral equation (VIE) on V for the total electric field can be rigorously expressed as [16]

$$\vec{E}^{\text{tot}}(\vec{r}) = \vec{E}^i(\vec{r}) + k_0^2 \int_V \left[\varepsilon_r(\vec{r}') - 1 \right] \vec{E}^{\text{tot}}(\vec{r}') \cdot \overline{\overline{G}}(\vec{r},\vec{r}') \, dv', \tag{2}$$

where $\vec{r} \in V$ and $k_0 = \omega\sqrt{\mu_0\varepsilon_0}$, which implies that

$$\vec{E}^s(\vec{r}) = \int_V \left(k_0^2 + \nabla\nabla\cdot \right) G(\vec{r},\vec{r}') \kappa(\vec{r}') \frac{\vec{D}^{\text{tot}}(\vec{r}')}{\varepsilon_0} dv', \tag{3}$$

where $\vec{D}^{\text{tot}}$ is the electric flux density of $\vec{E}^{\text{tot}}$ and

$$\kappa(\vec{r}') = \frac{\left(\varepsilon_r(\vec{r}') - 1\right)}{\varepsilon_r(\vec{r}')}. \tag{4}$$

Therefore, we have

$$\begin{aligned}
\vec{E}^s(\vec{r}) = \ & k_0^2 \int_V G(\vec{r},\vec{r}') \kappa(\vec{r}') \frac{\vec{D}^{\text{tot}}(\vec{r}')}{\varepsilon_0} dv' \\
& - \nabla \int_{\partial V} G(\vec{r},\vec{r}') \kappa(\vec{r}') \left[\hat{n}_{\partial V} \cdot \frac{\vec{D}^{\text{tot}}(\vec{r}')}{\varepsilon_0} \right] ds' \\
& + \nabla \int_V G(\vec{r},\vec{r}') \left[\kappa(\vec{r}') \left(\nabla' \cdot \frac{\vec{D}^{\text{tot}}(\vec{r}')}{\varepsilon_0} \right) \right. \\
& \left. + \frac{\vec{D}^{\text{tot}}(\vec{r}')}{\varepsilon_0} \cdot \nabla'\kappa(\vec{r}') \right] dv',
\end{aligned} \tag{5}$$

where ∂V is the outer boundary surface of V.

It should be pointed out that the second term in the right-hand side of (5) cannot be ignored in the strict sense (see the second paragraph of Section 2 in [17]). However, this term will force one to introduce "half" basis function, which will be seen in the following.

2.2. Buiding the MoM Model. The electric flux density $\vec{D}^{\text{tot}}$ can be chosen as the unknown function because it is continuous along the normal direction of the medium interface. After V is discretized by using tetrahedrons, $\vec{D}^{\text{tot}}/\varepsilon_0$ can be expanded with the SWG functions [1]:

$$\frac{\vec{D}^{\text{tot}}(\vec{r})}{\varepsilon_0} = \sum_{m=1}^{N_F} x_m^F \vec{f}_m^F(\vec{r}) + \sum_{n=1}^{N_H} x_n^H \vec{f}_n^H(\vec{r}), \tag{6}$$

where "F" and "H" mean "full SWG function" and "half SWG function," respectively, and the total number of the basis functions is $N = N_F + N_H$. A full SWG function $\vec{f}_n^F$ is defined on the union $V_n^F = V_n^{F,+} \cup V_n^{F,-}$ of a pair of tetrahedrons $V_n^{F,+}$ and $V_n^{F,-}$ that share a common face as follows:

$$\vec{f}_n^F(\vec{r}) = \begin{cases} \vec{f}_n^{F,+}(\vec{r}) = \dfrac{|S_n|}{3\,|V_n^+|}\left(\vec{r} - \vec{r}_{n,\text{free}}^+\right), & \vec{r} \in V_n^{F,+} \\[2mm] \vec{f}_n^{F,-}(\vec{r}) = \dfrac{|S_n|}{3\,|V_n^-|}\left(\vec{r} - \vec{r}_{n,\text{free}}^-\right), & \vec{r} \in V_n^{F,-}, \end{cases} \tag{7}$$
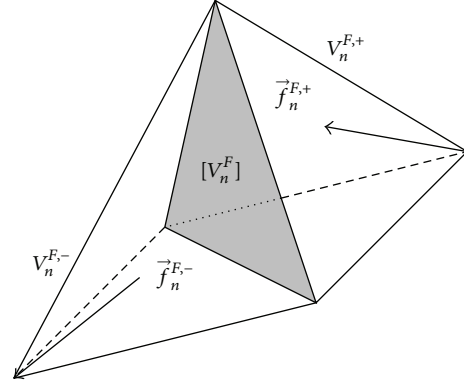

FIGURE 1: The geometry of the SWG function.

whose geometry is shown in Figure 1, while a half SWG function $\vec{f}_n^H$ is defined only on a single tetrahedron V_n^H. For convenience, we use $[V_n^F]$ to denote the common face of $V_n^{F,+}$ and $V_n^{F,-}$, as shown in Figure 1.

In fact, half SWG functions are applied only at the outer boundary of V, and hence the number N_H is just that of the triangular elements over ∂V. In this paper, we have a convention that a half SWG function $\vec{f}_n^H$ is so defined on V_n^H that $\vec{f}_n^H(\vec{r}) \cdot \hat{n}(\vec{r}) = 1$ when $\vec{r} \in [V_n^H] := V_n^H \cap \partial V$.

When (6) is substituted into (1) and after the Galerkin procedure is applied, the VIE-MoM matrix equation can be built as follows:

$$AX = B, \tag{8}$$

where

$$A = \begin{bmatrix} \left(a_{mn}^{FF}\right)_{N_F \times N_F} & \left(a_{mn}^{FH}\right)_{N_F \times N_H} \\ \left(a_{mn}^{HF}\right)_{N_H \times N_F} & \left(a_{mn}^{HH}\right)_{N_H \times N_H} \end{bmatrix};$$

$$B = \begin{bmatrix} \left(b_m^F\right)_{N_F \times 1} \\ \left(b_m^H\right)_{N_H \times 1} \end{bmatrix} \text{ is the incident vector;} \tag{9}$$

$$X = \begin{bmatrix} \left(x_n^F\right)_{N_F \times 1} \\ \left(x_n^H\right)_{N_H \times 1} \end{bmatrix} \text{ is the unknown vector.}$$

Note that, in our VIE-MoM model, the restriction of $\kappa(\vec{r})$ on a tetrahedral region will be considered as a constant, and the following symbol abbreviations will be applied:

$$\kappa_n^{F,\pm} := \kappa(\vec{r})\,|_{V_n^{F,\pm}}, \qquad \kappa_n^H := \kappa(\vec{r})\,|_{V_n^H}. \tag{10}$$

Then the elements of matrix A have the following expressions:

$$\begin{aligned}
a_{mn}^{FF} = \ & \int_{V_m^F} \frac{\vec{f}_m^F(\vec{r}) \cdot \vec{f}_n^F(\vec{r})}{\varepsilon_r(\vec{r})} dv \\
& - k_0^2 \int_{V_m^F} dv \vec{f}_m^F(\vec{r}) \cdot \int_{V_n^F} G(\vec{r},\vec{r}') \kappa(\vec{r}') \vec{f}_n^F(\vec{r}') dv'
\end{aligned}$$

$$+ \int_{V_m^F} dv \left(\nabla \cdot \vec{f}_m^F \left(\vec{r} \right) \right) \left\{ I_{mn}^{F,(1)} \left(\vec{r} \right) + I_{mn}^{F,(2)} \left(\vec{r} \right) \right\}$$

$$:= a_{mn}^{FF,1} - k_0^2 a_{mn}^{FF,2} + a_{mn}^{FF,3}, \tag{11}$$

$$a_{mn}^{HF} = \int_{V_m^H} \frac{\vec{f}_m^H \left(\vec{r} \right) \cdot \vec{f}_n^F \left(\vec{r} \right)}{\varepsilon_r \left(\vec{r} \right)} dv$$

$$- k_0^2 \int_{V_m^H} dv \vec{f}_m^H \left(\vec{r} \right) \cdot \int_{V_n^F} G \left(\vec{r}, \vec{r}' \right) \kappa \left(\vec{r}' \right) \vec{f}_n^F \left(\vec{r}' \right) dv'$$

$$+ \left[\int_{V_m^H} dv \left(\nabla \cdot \vec{f}_m^H \left(\vec{r} \right) \right) \left\{ I_{mn}^{F,(1)} \left(\vec{r} \right) + I_{mn}^{F,(2)} \left(\vec{r} \right) \right\} \right.$$

$$\left. - \int_{[V_n^H]} ds \left\{ I_{mn}^{F,(1)} \left(\vec{r} \right) + I_{mn}^{F,(2)} \left(\vec{r} \right) \right\} \right]$$

$$:= a_{mn}^{HF,1} - k_0^2 a_{mn}^{HF,2} + a_{mn}^{HF,3}, \tag{12}$$

where

$$I_{mn}^{F,(1)} \left(\vec{r} \right) = \int_{V_n^F} G \left(\vec{r}, \vec{r}' \right) \kappa \left(\vec{r}' \right) \left(\nabla' \cdot \vec{f}_n^F \left(\vec{r}' \right) \right) dv',$$

$$I_{mn}^{F,(2)} \left(\vec{r} \right) = \int_{[V_n^F]} G \left(\vec{r}, \vec{r}' \right) \left[\kappa_n^{F,-} - \kappa_n^{F,+} \right] ds'. \tag{13}$$

Note that $a_{mn}^{FF,1} = 0$ in (11) when V_m^F and V_n^F are properly separated and that $a_{mn}^{HF,1} = 0$ in (12) when V_m^H and V_n^F are properly separated:

$$a_{mn}^{FH} = \int_{V_m^F} \frac{\vec{f}_m^F \left(\vec{r} \right) \cdot \vec{f}_n^H \left(\vec{r} \right)}{\varepsilon_r \left(\vec{r} \right)} dv$$

$$- k_0^2 \int_{V_m^F} dv \vec{f}_m^F \left(\vec{r} \right) \cdot \int_{V_n^H} G \left(\vec{r}, \vec{r}' \right) \kappa \left(\vec{r}' \right) \vec{f}_n^H \left(\vec{r}' \right) dv'$$

$$+ \int_{V_m^F} dv \left(\nabla \cdot \vec{f}_m^F \left(\vec{r} \right) \right) \left\{ I_{mn}^{H,(1)} \left(\vec{r} \right) - I_{mn}^{H,(2)} \left(\vec{r} \right) \right\}$$

$$:= a_{mn}^{FH,1} - k_0^2 a_{mn}^{FH,2} + a_{mn}^{FH,3}, \tag{14}$$

$$a_{mn}^{HH} = \int_{V_m^H} \frac{\vec{f}_m^H \left(\vec{r} \right) \cdot \vec{f}_n^H \left(\vec{r} \right)}{\varepsilon_r \left(\vec{r} \right)} dv$$

$$- k_0^2 \int_{V_m^H} dv \vec{f}_m^H \left(\vec{r} \right) \cdot \int_{V_n^H} G \left(\vec{r}, \vec{r}' \right) \kappa \left(\vec{r}' \right) \vec{f}_n^H \left(\vec{r}' \right) dv'$$

$$+ \left[\int_{V_m^H} dv \left(\nabla \cdot \vec{f}_m^H \left(\vec{r} \right) \right) \left\{ I_{mn}^{H,(1)} \left(\vec{r} \right) - I_{mn}^{H,(2)} \left(\vec{r} \right) \right\} \right.$$

$$\left. - \int_{[V_m^H]} ds \left\{ I_{mn}^{H,(1)} \left(\vec{r} \right) - I_{mn}^{H,(2)} \left(\vec{r} \right) \right\} \right]$$

$$:= a_{mn}^{HH,1} - k_0^2 a_{mn}^{HH,2} + a_{mn}^{HH,3}, \tag{15}$$

where

$$I_{mn}^{H,(1)} \left(\vec{r} \right) = \int_{V_n^H} G \left(\vec{r}, \vec{r}' \right) \kappa \left(\vec{r}' \right) \left(\nabla' \cdot \vec{f}_n^H \left(\vec{r}' \right) \right) dv',$$

$$I_{mn}^{H,(2)} \left(\vec{r} \right) = \int_{[V_n^H]} ds' G \left(\vec{r}, \vec{r}' \right) \kappa \left(\vec{r}' \right). \tag{16}$$

Note that $a_{mn}^{FH,1} = 0$ in (14) when V_m^F and V_n^H are properly separated and that $a_{mn}^{HH,1} = 0$ in (15) when V_m^H and V_n^H are properly separated.

2.3. The Frame for the VIE-FG-FFT.

In this section, the FG-FFT technology is introduced into the VIE-MoM for both reducing memory requirement and improving computational efficiency.

The entire MoM matrix A can be split into two parts: the near-field matrix A^{near} and the far-field matrix A^{far}, and

$$A = \left(A - A^{far} \right) + A^{far} \simeq A^{near} + A^{far}, \tag{17}$$

where the A^{near} is a sparse matrix (the identification of a near-element will be presented in the second paragraph of Section 3), which is obtained by forcing all "far elements" of $A - A^{far}$ to be equal to zero, and A^{far} can ultimately expressed in such a form as follows:

$$A^{far} = -k_0^2 \vec{\Pi}_f \cdot G \vec{\Pi}_c^T + \Pi_f G \Pi_c^T, \tag{18}$$

where $\vec{\Pi}_f$, $\vec{\Pi}_c$, Π_f, and Π_c are all sparse matrices which will be constructed in Section 2.4 and where the head mark " $\rightarrow$ " implies matrix elements being 3D vectors; G is a triple Toeplitz matrix related to Green's function; the superscript T indicates matrix transpose.

When an iterative solver is applied, the matrix-vector product will be performed by means of

$$Ax \simeq A^{near} x + A^{far} x, \tag{19}$$

where $A^{near} x$ is directly calculated, while $A^{far} x$ can be speeded up by means of the FFT through (18). In this way, the VIE-FG-FFT can reduce the memory requirement and the computational complexity to $O(N)$ and $O(N \log(N))$ theoretically (also see [9] for more detailed analysis).

2.4. Fitting Green's Function.

In this section, matrices $\vec{\Pi}_f$, $\vec{\Pi}_c$, Π_f, and Π_c in (18) will be constructed. First, let a uniform Cartesian grid enclose the given volumetric region V. Use h_x, h_y, and h_z to denote the three grid spacing sizes in the directions $\hat{x}$, $\hat{y}$, and $\hat{z}$, respectively. In this paper, however, the convention $h := h_x = h_y = h_z$ is always selected.

In a uniform Cartesian grid, an *expansion box* (or simply *box*) $\mathbf{C}$ is defined as a cube-like collection composed of $(M_x + 1) \times (M_y + 1) \times (M_z + 1)$ nodes. When $M_x = M_y = M_z = M$, $\mathbf{C}$ includes $(M+1)^3$ nodes and M is called its *expansion order* (or simply *order*), written as $|\mathbf{C}|$. Figure 2 illustrates a box of order 2.

TABLE 1: Correspondences between integral regions and Gaussian points and weights.

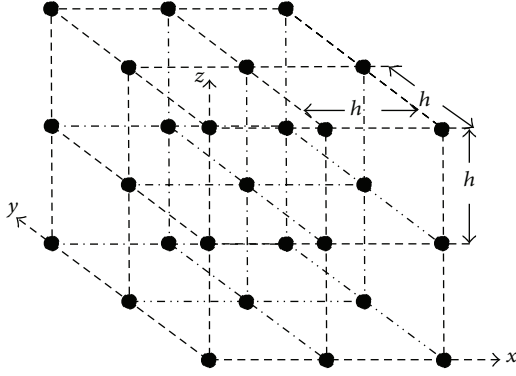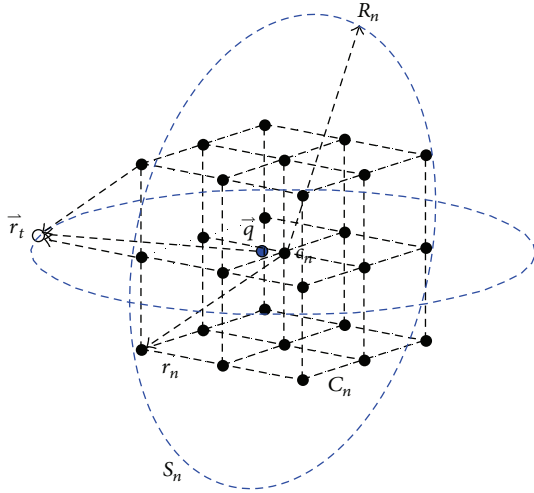| Integral region	$V_m^{F,\pm}$	V_m^H	$[V_m^F]$	$V_n^{F,\pm}$	V_n^H	$[V_n^H]$
Gaussian points	$\{\vec{p}_i^{\,\pm}\}_{i=1}^{N_G}$	$\{\vec{p}_i\}_{i=1}^{N_G}$	$\{\vec{s}_i\}_{i=1}^{M_G}$	$\{\vec{q}_j^{\,\pm}\}_{j=1}^{N_G}$	$\{\vec{q}_j\}_{j=1}^{N_G}$	$\{\vec{t}_j\}_{j=1}^{M_G}$
Gaussian weights		$\{w_i\}_{i=1}^{N_G}$	$\{\widehat{w}_i\}_{i=1}^{M_G}$		$\{w_j\}_{j=1}^{N_G}$	$\{\widehat{w}_j\}_{j=1}^{M_G}$

FIGURE 2: An expansion box of order 2.

FIGURE 3: A 3D representation of the matching Green's function.

Assume that $\mathbf{C}_n$ is a box centered at c_n of radius r_n and $\vec{q}$ is a fixed point within $\mathbf{C}_n$. Let Green's function be represented into

$$G(\vec{r}, \vec{q}) = \sum_{\mathbf{v} \in \mathbf{C}_n} \pi_{\mathbf{v}, \mathbf{C}_n}^{\vec{q}} G(\vec{r}, \mathbf{v}), \qquad (20)$$

where the coefficients $\pi_{\mathbf{v}, \mathbf{C}_n}^{\vec{q}}$ are to be determined and $\vec{r}$ is an arbitrary point outside the box $\mathbf{C}_n$, as shown in Figure 3.

Now we select a spherical surface with the center at c_n and the radius R_n slightly larger than r_n, and select a group of sample points $\{\vec{r}_t\}_{t=1}^T$ on the surface [18], where the number T ought to be significantly greater than that of the nodes within $\mathbf{C}_n$. In this paper, $R_n - r_n = 0.15$ wavelength, which was adopted in [15]. Then we match Green's function values at these sample points. The resultant systems of matrix

equations can be solved by the least-square method [19]. In this paper, the order of a box is selected to be 2, and at this time the number of sample points on the testing spherical surface is selected to be 120.

Without loss of generality, assume that $V_m^{F,\pm}$ and V_m^H ($V_n^{F,\pm}$ and V_n^H) are in box $\mathbf{C}_m$ ($\mathbf{C}_n$). Calculations of MoM matrix elements ultimately come down to calculations on the Gaussian points. We specify using N_G Gaussian points in a tetrahedral region and M_G Gaussian points in a triangular region. For convenience, the correspondences between integral regions and Gaussian points and weights that will be used are all listed in Table 1. When the testing element and the source element are separated by a proper distance, all the first terms in the right-hand side of (11), (12), (14), and (15) will vanish. At this case, we can easily obtain the following approximate expressions:

$$
\begin{aligned}
a_{mn}^{FF,2} &= \sum_{\mathbf{u} \in \mathbf{C}_m} \sum_{\mathbf{v} \in \mathbf{C}_n} \vec{\pi}_{\mathbf{u},\mathbf{C}_m}^{\vec{f}_m^F, f} \cdot G(\mathbf{u}, \mathbf{v}) \, \vec{\pi}_{\mathbf{v},\mathbf{C}_n}^{\vec{f}_n^F, c}, \\
a_{mn}^{FF,3} &= \sum_{\mathbf{u} \in \mathbf{C}_m} \sum_{\mathbf{v} \in \mathbf{C}_n} \pi_{\mathbf{u},\mathbf{C}_m}^{\vec{f}_m^F, f} G(\mathbf{u}, \mathbf{v}) \, \pi_{\mathbf{v},\mathbf{C}_n}^{\vec{f}_n^F, c}, \\
a_{mn}^{HF,2} &= \sum_{\mathbf{u} \in \mathbf{C}_m} \sum_{\mathbf{v} \in \mathbf{C}_n} \vec{\pi}_{\mathbf{u},\mathbf{C}_m}^{\vec{f}_m^H, f} \cdot G(\mathbf{u}, \mathbf{v}) \, \vec{\pi}_{\mathbf{v},\mathbf{C}_n}^{\vec{f}_n^F, c}, \\
a_{mn}^{HF,3} &= \sum_{\mathbf{u} \in \mathbf{C}_m} \sum_{\mathbf{v} \in \mathbf{C}_n} \pi_{\mathbf{u},\mathbf{C}_m}^{\vec{f}_m^H, f} G(\mathbf{u}, \mathbf{v}) \, \pi_{\mathbf{v},\mathbf{C}_n}^{\vec{f}_n^F, c}, \\
a_{mn}^{FH,2} &= \sum_{\mathbf{u} \in \mathbf{C}_m} \sum_{\mathbf{v} \in \mathbf{C}_n} \vec{\pi}_{\mathbf{u},\mathbf{C}_m}^{\vec{f}_m^F, f} \cdot G(\mathbf{u}, \mathbf{v}) \, \vec{\pi}_{\mathbf{v},\mathbf{C}_n}^{\vec{f}_n^H, c}, \\
a_{mn}^{FH,3} &= \sum_{\mathbf{u} \in \mathbf{C}_m} \sum_{\mathbf{v} \in \mathbf{C}_n} \pi_{\mathbf{u},\mathbf{C}_m}^{\vec{f}_m^F, f} G(\mathbf{u}, \mathbf{v}) \, \pi_{\mathbf{v},\mathbf{C}_n}^{\vec{f}_n^H, c}, \\
a_{mn}^{HH,2} &= \sum_{\mathbf{u} \in \mathbf{C}_m} \sum_{\mathbf{v} \in \mathbf{C}_n} \vec{\pi}_{\mathbf{u},\mathbf{C}_m}^{\vec{f}_n^H, f} \cdot G(\mathbf{u}, \mathbf{v}) \, \vec{\pi}_{\mathbf{v},\mathbf{C}_n}^{\vec{f}_n^H, c}, \\
a_{mn}^{HH,3} &= \sum_{\mathbf{u} \in \mathbf{C}_m} \sum_{\mathbf{v} \in \mathbf{C}_n} \pi_{\mathbf{u},\mathbf{C}_m}^{\vec{f}_m^H, f} G(\mathbf{u}, \mathbf{v}) \, \pi_{\mathbf{v},\mathbf{C}_n}^{\vec{f}_n^H, c},
\end{aligned}
\tag{21}
$$

where the coefficients are calculated by using the following formulae:

$$\vec{\pi}_{\mathbf{u},\mathbf{C}_m}^{\vec{f}_m^F, f} = \sum_{i=1}^{N_G} w_i \left[\vec{f}_m^{F,+}(\vec{p}_i^+) \, \pi_{\mathbf{u},\mathbf{C}_m}^{\vec{p}_i^+} + \vec{f}_m^{F,-}(\vec{p}_i^-) \, \pi_{\mathbf{u},\mathbf{C}_m}^{\vec{p}_i^-} \right],$$

$$\pi_{\mathbf{u},\mathbf{C}_m}^{\vec{f}_m^F, f} = \sum_{i=1}^{N_G} w_i \left\{ \left[\nabla \cdot \vec{f}_m^{F,+}(\vec{p}_i^+) \right] \pi_{\mathbf{u},\mathbf{C}_m}^{\vec{p}_i^+} \right.$$

$$\left. + \left[\nabla \cdot \vec{f}_m^{F,-}(\vec{p}_i^-) \right] \pi_{\mathbf{u},\mathbf{C}_m}^{\vec{p}_i^-} \right\},$$

$$\vec{\pi}_{\mathbf{v},\mathbf{C}_n}^{\vec{f}_n^F,c} = \sum_{j=1}^{N_G} w_j \left[\kappa_n^{F,+} \vec{f}_n^{F,+} \left(\vec{q}_j^+ \right) \pi_{\mathbf{v},\mathbf{C}_n}^{\vec{q}_j^+} \right.$$

$$\left. + \kappa_n^{F,-} \vec{f}_n^{F,-} \left(\vec{q}_j^- \right) \pi_{\mathbf{v},\mathbf{C}_n}^{\vec{q}_j^-} \right],$$

$$\pi_{\mathbf{v},\mathbf{C}_n}^{\vec{f}_n^F,c} = \sum_{j=1}^{N_G} w_j \left\{ \kappa_n^{F,+} \left[\nabla \cdot \vec{f}_n^{F,+} \left(\vec{q}_j^+ \right) \right] \pi_{\mathbf{v},\mathbf{C}_n}^{\vec{q}_j^+} \right.$$

$$\left. + \kappa_n^{F,-} \left[\nabla \cdot \vec{f}_n^{F,-} \left(\vec{q}_j^- \right) \right] \pi_{\mathbf{v},\mathbf{C}_n}^{\vec{q}_j^-} \right\}$$

$$+ \sum_{j=1}^{M_G} \widehat{w}_j \left[\kappa_n^{F,-} - \kappa_n^{F,+} \right] \pi_{\mathbf{v},\mathbf{C}_n}^{\vec{t}_j},$$

$$\vec{\pi}_{\mathbf{u},\mathbf{C}_m}^{\vec{f}_m^H,f} = \sum_{i=1}^{N_G} w_i \vec{f}_m^H \left(\vec{p}_i \right) \pi_{\mathbf{u},\mathbf{C}_m}^{\vec{p}_i},$$

$$\pi_{\mathbf{u},\mathbf{C}_m}^{\vec{f}_m^H,f} = \sum_{i=1}^{N_G} w_i \left[\nabla \cdot \vec{f}_m^H \left(\vec{p}_i \right) \right] \pi_{\mathbf{u},\mathbf{C}_n}^{\vec{p}_i} - \sum_{i=1}^{M_G} \widehat{w}_i \pi_{\mathbf{u},\mathbf{C}_m}^{\vec{s}_i},$$

$$\vec{\pi}_{\mathbf{v},\mathbf{C}_n}^{\vec{f}_n^H,c} = \sum_{j=1}^{N_G} w_j \kappa_n^H \vec{f}_n^H \left(\vec{q}_j \right) \pi_{\mathbf{v},\mathbf{C}_n}^{\vec{q}_j},$$

$$\pi_{\mathbf{v},\mathbf{C}_n}^{\vec{f}_n^H,c} = \sum_{j=1}^{N_G} w_j \kappa_n^H \left[\nabla \cdot \vec{f}_n^H \left(\vec{q}_j \right) \right] \pi_{\mathbf{v},\mathbf{C}_n}^{\vec{q}_j} - \sum_{j=1}^{M_G} \widehat{w}_j \kappa_n^H \pi_{\mathbf{v},\mathbf{C}_n}^{\vec{t}_j}.$$

$$(22)$$

Substituting (21) into (11)–(16), we can easily obtain formula (18). It should be pointed out that performing matrix-vector product $A^{\text{far}} x$ once based on (18) requires at least 8 FFTs.

2.5. On the Preprocessing Time. Here, the preprocessing time means the time taken by generating the coefficients in (21). Clearly, the preprocessing time is proportional to the corresponding computational complexity. For general cases, from the coefficient formulae in Section 2.4, it can be evaluated that the number $N_{\text{FG-FFT}}$ of required float multiplications is about

$$N_{\text{FG-FFT}}$$
$$= N_F \left(22 N_G + 5 M_G + 24 \right) + N_H \left(11 N_G + 2 M_G + 15 \right).$$
$$(23)$$

In the VIE-P-FFT, the corresponding coefficients are generated by utilizing "projecting coefficients," which requires solving the least-square problem with multiple right-hand terms. If the order of a box is selected to be 2, containing 27 grid points, and the number of the sample points on the testing spherical surface is selected to be T, then the matrix of the least-square problem in whether the VIE-P-FFT or the VIE-FG-FFT is a $T \times 27$ complex matrix. Further, if the SVD process of the matrix is ignored, then the least-square solution for a right-hand term requires about $T^2 + 27^2$ complex multiplications or about $3(T^2 + 27^2)$ real
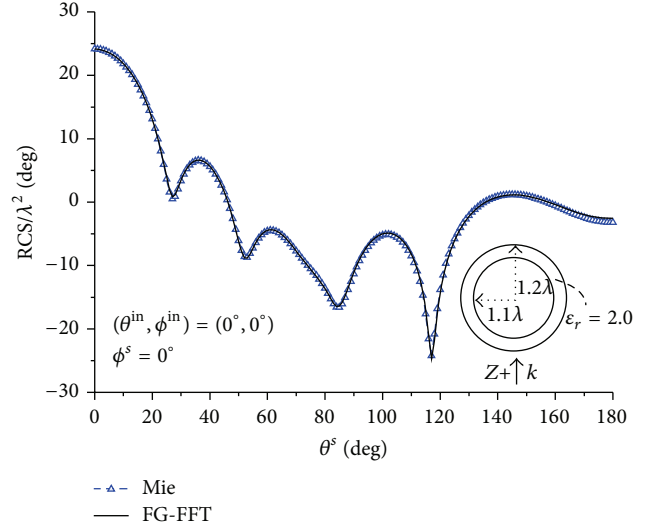

FIGURE 4: Bistatic RCS curves of the dielectric spherical shell in Example A.

multiplications because a complex multiplication requires at least 3 real multiplications. It is easily known from the projection scheme introduced in [20] that, for generating the corresponding coefficients, the number $N_{\text{P-FFT}}$ of required float multiplications is about

$$N_{\text{P-FFT}} = 24 N \left(T^2 + 27^2 \right), \qquad (24)$$

which is usually much larger than $N_{\text{FG-FFT}}$.

It can be concluded from the above analysis that the preprocessing time of the VIE-FG-FFT is obviously less than that of the VIE-P-FFT for inhomogeneous nonmagnetic dielectric objects.

3. Numerical Results

In this section, several examples are provided to demonstrate the validity, accuracy, and efficiency of the VIE-FG-FFT. In all the examples, the expansion order M is always chosen as 2, and the Cartesian grid spacing sizes in different directions are always selected to be the same as each other; namely, $h := h_x = h_y = h_z$. Besides, λ denotes the wavelength in free space. Our computing platform is a DELL T5400 workstation with 8 cores of clock frequency 3 GHz, and the FFT codes are from the FFTW [21].

Assume that the testing function and the source function are located within boxes $\mathbf{C}_m$ and $\mathbf{C}_n$, respectively. Then the corresponding matrix element is identified as a *near element* if and only if the distance between the center of $\mathbf{C}_m$ and that of $\mathbf{C}_n$ is smaller than the sum of the radius of $\mathbf{C}_m$ and that of $\mathbf{C}_n$.

3.1. Example A: Homogeneous Ball. A dielectric spherical shell with the relative permittivity 2.0 is considered, as shown in Figure 4. This object is discretized by using 23174 tetrahedrons with the average edge length 0.1λ, producing 51231 unknowns. The Cartesian grid spacing size is chosen as $h = 0.1\lambda$.
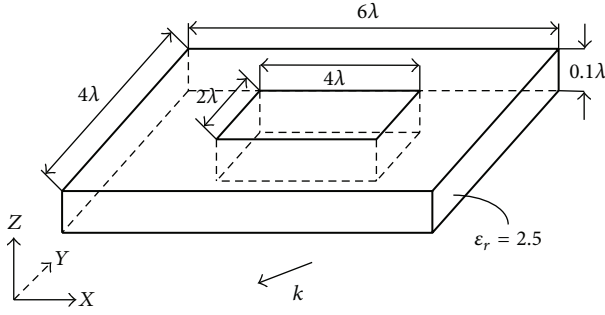
FIGURE 5: The dimensions of the hollow dielectric slab in Example B.

TABLE 2: RMSEs of the RCSs in Example B.

Method	$h(\lambda)$	RMSE	$h(\lambda)$	RMSE	$h(\lambda)$	RMSE
FG-FFT	0.1	0.0943	0.15	0.2004	0.2	0.5062
AIM	0.1	0.3895	0.15	0.9826	0.2	2.7141
IE-FFT	0.1	0.4415	0.15	1.0912	0.2	2.9753
P-FFT	0.1	0.0986	0.15	0.2048	0.2	0.5124

The bistatic RCS curve obtained by the FG-FFT is compared with the Mie series solution in Figure 4. It can be seen that the two curves coincide very well, which demonstrates the validity of the FG-FFT.

3.2. Example B: Homogeneous Slab. A homogeneous hollow dielectric slab with the relative permittivity 2.5 is considered, as shown in Figure 5. The direction of the incident wave is $(\theta^{in}, \varphi^{in}) = (90°, 45°)$. This object is discretized by using 19301 tetrahedrons with the average edge length 0.1λ, producing 42862 unknowns. The Cartesian grid spacing size is chosen as $h = 0.1\lambda, 0.15\lambda$, and 0.2λ, respectively.

The bistation RCS curves obtained by the direct MoM, the FG-FFT, and the other FFT-based methods (the P-FFT, the AIM, and the IE-FFT) are all shown in Figure 6, and the RMSEs are recorded in Table 2, which are calculated by the following formula:

$$\text{RMSE} = \sqrt{\frac{1}{N} \sum_{m=1}^{N} \left| \text{RCS}^{\text{FFT-based}} - \text{RCS}^{\text{MoM}} \right|^2}, \quad (25)$$

where N is the number of sampling theta azimuth angles. In this example, $N = 100$.

It can be seen from Figure 6 and Table 2 that when the grid spacing size is $h = 0.1\lambda$, the four RCS curves obtained by the FG-FFT, P-FFT, IE-FFT, and AIM agree well with that by the direct MoM. However, when increasing the grid spacing size gradually, both the FG-FFT and P-FFT can keep consistent with the MoM, while both the P-FFT and IE-FFT do not.

It can be concluded from the above experiments that compared with both the AIM and IE-FFT, both the FG-FFT and P-FFT are more accurate and not sensitive to the Cartesian grid spacing size.

TABLE 3: RMSEs of the RCSs in Example C.

Method	$h(\lambda)$	RMSE	$h(\lambda)$	RMSE	$h(\lambda)$	RMSE
FG-FFT	0.1	0.0704	0.15	0.1579	0.2	0.4854
AIM	0.1	0.3771	0.15	0.5648	0.2	1.2602
IE-FFT	0.1	0.4529	0.15	0.6406	0.2	1.3502
P-FFT	0.1	0.0738	0.15	0.1614	0.2	0.4936

TABLE 4: The Preprocessing time in Example D.

Method	Edge length (λ)	Unknowns	Preprocessing time (s)
FG-FFT	0.15	10875	18.42
P-FFT			84.36
FG-FFT	0.1	39927	261.27
P-FFT			512.69
FG-FFT	0.08	61376	934.07
P-FFT			1326.58

3.3. Example C: Partitioned Homogeneous Slab. A partitioned homogeneous hollow dielectric slab with 4 different relative permittivities is considered, as shown in Figure 7. The direction of the incident wave is $(\theta^{in}, \varphi^{in}) = (90°, 45°)$. This object is discretized by using 17714 tetrahedrons with the average edge length 0.1λ, producing 39927 unknowns. The Cartesian grid spacing size is chosen as $h = 0.1\lambda, 0.15\lambda$, and 0.2λ, respectively.

The bistatic RCS curves obtained by the direct MoM, the FG-FFT, and other FFT-based methods are all shown in Figure 8, and the RMSEs are recorded in Table 3. In this example, $N = 100$ for the RMSE.

It is again seen from Figure 8 and Table 3 that the accuracy of both the FG-FFT and P-FFT is higher than that of both the IE-FFT and AIM.

3.4. Example D: Inhomogeneous Slab. Here the dielectric slab in Figure 5 is again considered. The direction of the incident wave is kept unchanged. But at this time, the relative permittivity

$$\varepsilon_r(x, y, z) = \varepsilon_r'(x, y, z) - j\varepsilon_r''(x, y, z) \quad (26)$$

is defined by

$$\varepsilon_r'(x, y, z) = 0.2 \frac{x + y + z}{10.1} + 2.0,$$
$$\varepsilon_r''(x, y, z) = 0.1, \quad (27)$$

where $x, y, z \geq 0$. Now, the average edge length used in the discretization is selected within $\{0.08\lambda, 0.1\lambda, 0.15\lambda\}$.

Different discretization granularities correspond to different numbers of unknowns, as shown in Table 4. The bistatic RCS curves obtained by the FG-FFT and P-FFT for different discretization granularities are all shown in Figure 9, and the preprocessing time for the FG-FFT and P-FFT is recorded in Table 4.

It can be seen from Figure 9 that the RCS curves for different discretization granularities are almost the same as each
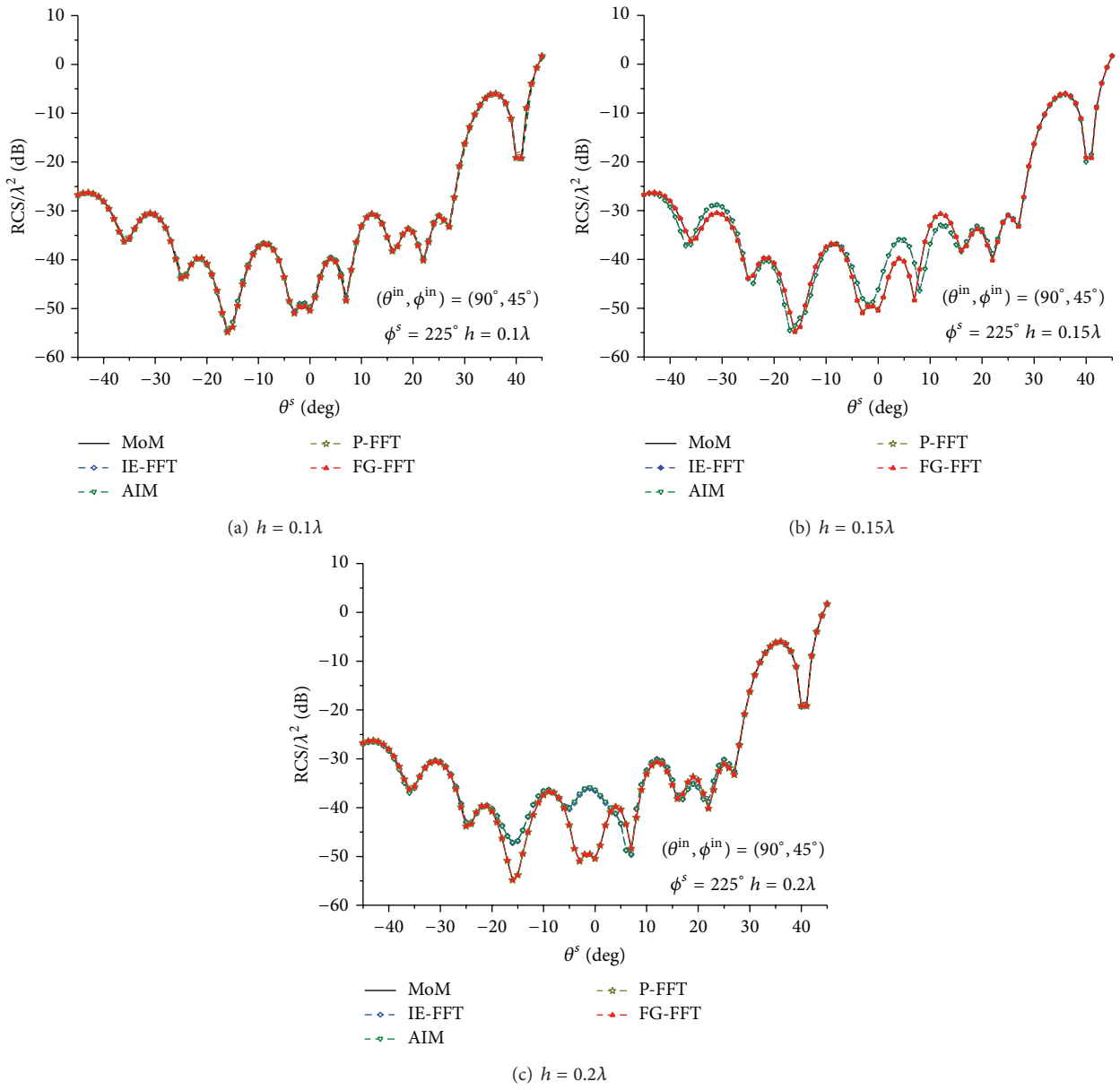
(a) $h = 0.1\lambda$

(b) $h = 0.15\lambda$

(c) $h = 0.2\lambda$

FIGURE 6: Bistatic RCS curves of the homogeneous dielectric slab in Example B.
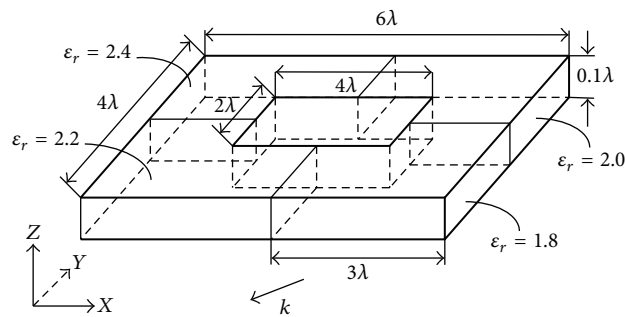
FIGURE 7: The dimensions of the hollow dielectric slab in Example C.

(a) $h = 0.1\lambda$

(b) $h = 0.15\lambda$

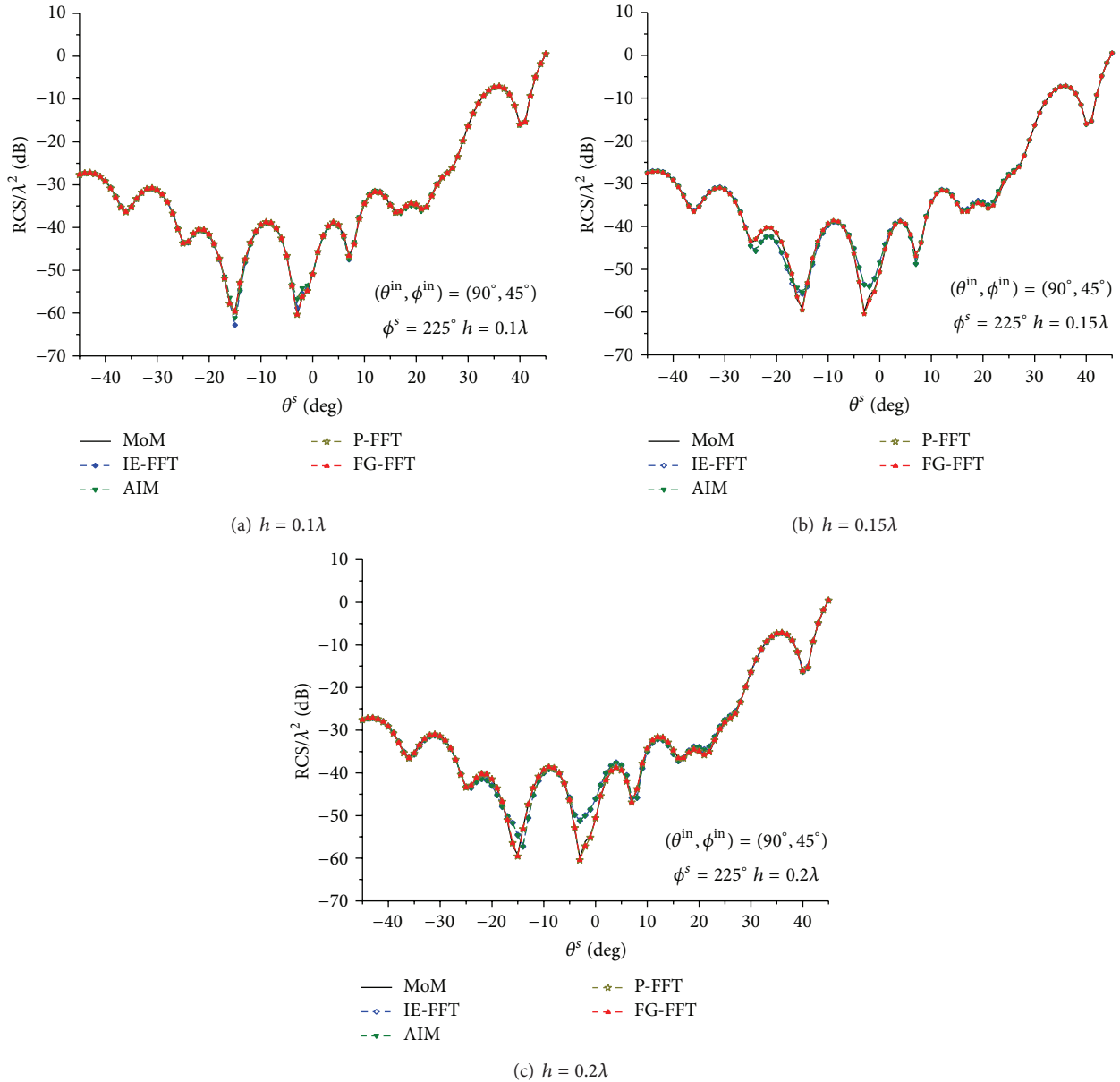(c) $h = 0.2\lambda$

Figure 8: Bistatic RCS curves of the partitioned homogeneous dielectric slab in Example C.

other. It can be known from Table 4 that the preprocessing time of the FG-FFT is obviously less than that of the P-FFT for different discretization granularities.

4. Conclusions

In this paper, a new realization of the VIE combined with the fast Fourier transform (VIE-FG-FFT) has been established to solve EM scattering from inhomogeneous nonmagnetic dielectric objects. The proposed method has been compared with several existing popular FFT-based methods, including the VIE-P-FFT, VIE-AIM, and VIE-IE-FFT. The accuracy of the VIE-FG-FFT is almost the same as that of the VIE-P-FFT and higher than that of the VIE-AIM and VIE-IE-FFT

especially when increasing the grid spacing size. Besides, the preprocessing time of the VIE-FG-FFT is obviously less than that of the P-FFT for inhomogeneous nonmagnetic dielectric objects.

Conflict of Interests

The authors declare that there is no conflict of interests regarding the publication of this paper.

Acknowledgments
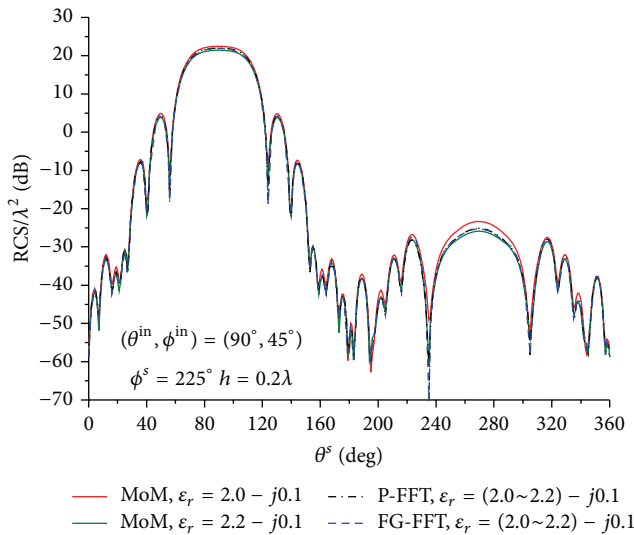
FIGURE 9: Bistatic RCS curves of the inhomogeneous dielectric slab ($h = 0.2\lambda$) in Example D.

References

[1] D. H. Schaubert, D. R. Wilton, and A. W. Glisson, "A tetrahedral modeling method for electromagnetic scattering arbitrarily shaped inhomogeneous dielectric bodies," *IEEE Transactions on Antennas and Propagation*, vol. 32, no. 1, pp. 77–85, 1984.

[2] R. F. Harrington, *Field Computation by Moment Methods*, The MacMillian, New York, NY, USA, 1968.

[3] Z. Q. Zhang and Q. H. Liu, "A Volume Adaptive Integral Method (VAIM) for 3-D inhomogeneous objects," *IEEE Antennas and Wireless Propagation Letters*, vol. 1, pp. 102–105, 2002.

[4] J.-L. Gou, J.-Y. Li, and Q.-Z. Liu, "Analysis of arbitrarily shaped dielectric radomes using adaptive integral method based on volume integral equation," *IEEE Transactions on Antennas and Propagation*, vol. 54, no. 7, pp. 1910–1916, 2006.

[5] X.-C. Nie, L.-W. Li, N. Yuan, T. S. Yeo, and Y.-B. Gan, "Precorrected-FFT solution of the volume integral equation for 3-D inhomogeneous dielectric objects," *IEEE Transactions on Antennas and Propagation*, vol. 53, no. 1, pp. 313–320, 2005.

[6] X.-C. Nie, N. Yuan, L.-W. Li, Y.-B. Gan, and T. S. Yeo, "A fast combined field volume integral equation solution to EM scattering by 3-D dielectric objects of arbitrary permittivity and permeability," *IEEE Transactions on Antennas and Propagation*, vol. 54, no. 3, pp. 961–969, 2006.

[7] N. A. Ozdemir and J.-F. Lee, "IE-FFT algorithm for a nonconformal volume integral equation for electromagnetic scattering from dielectric objects," *IEEE Transactions on Magnetics*, vol. 44, no. 6, pp. 1398–1401, 2008.

[8] J. Yin, J. Hu, H. Guo, and Z. Nie, "Fast analysis of 3D inhomogeneous dielectric objects using IE-FFT," *IEEE Transactions on Antennas and Propagation*, vol. 30, no. 5, pp. 409–418, 2009.

[9] E. Bleszynski, M. Bleszynski, and T. Jaroszewicz, "AIM: Adaptive integral method for solving large-scale electromagnetic scattering and radiation problems," *Radio Science*, vol. 31, no. 5, pp. 1225–1251, 1996.

[10] J. R. Phillips and J. K. White, "A Precorrected-FFT method for electrostatic analysis of complicated 3-D structures," *IEEE Transactions on Computer-Aided Design of Integrated Circuits and Systems*, vol. 16, no. 10, pp. 1059–1072, 1997.

[11] L.-W. Li, Y.-J. Wang, and E.-P. Li, "MPI-based parallelized precorrected FFT algorithm for analyzing scattering by arbitrarily shaped three-dimensional objects—abstract," *Journal of Electromagnetic Waves and Applications*, vol. 17, no. 10, pp. 1489–1491, 2003.

[12] S. M. Seo and J.-F. Lee, "A fast IE-FFT algorithm for solving PEC scattering problems," *IEEE Transactions on Magnetics*, vol. 41, no. 5, pp. 1476–1479, 2005.

[13] S. M. Rao, D. R. Wilton, and A. W. Glisson, "Electromagnetic scattering by surfaces of arbitrary shape," *IEEE Transactions on Antennas and Propagation*, vol. 30, no. 3, pp. 409–418, 1982.

[14] J.-Y. Xie, H.-X. Zhou, W. Hong, W.-D. Li, and G. Hua, "A novel FG-FFT method for the EFIE," in *Proceedings of the International Conference on Computational Problem-Solving (ICCP '12)*, pp. 111–115, October 2012.

[15] J.-Y. Xie, H.-X. Zhou, W. Hong, W.-D. Li, and G. Hua, "A highly accurate FGG-FG-FFT for the combined field integral equation," *IEEE Transactions on Antennas and Propagation*, vol. 61, no. 9, pp. 4641–4652, 2013.

[16] M. I. Sancer, K. Sertel, J. L. Volakis, and P. van Alstine, "On volume integral equations," *IEEE Transactions on Antennas and Propagation*, vol. 54, no. 5, pp. 1488–1495, 2006.

[17] C. C. Lu and W. C. Chew, "A coupled surface-volume integral equation approach for the calculation of electromagnetic scattering from composite metallic and material targets," *IEEE Transactions on Antennas and Propagation*, vol. 48, no. 12, pp. 1866–1868, 2000.

[18] A. D. McLaren, "Optimal numerical integration on a sphere," *Mathematics of Computation*, vol. 17, pp. 361–383, 1963.

[19] D. Kincaid and W. Cheney, *Numerical Analysis: Mathematics of Scientific Computing*, Brooks Cole, Pacific Grove, Calif, USA, 3rd edition, 2002.

[20] X.-C. Nie, L.-W. Li, N. Yuan, T. S. Yeo, and Y.-B. Gan, "Precorrected-FFT solution of the volume integral equation for 3-D inhomogeneous dielectric objects," *IEEE Transactions on Antennas and Propagation*, vol. 53, no. 1, pp. 313–320, 2005.

[21] M. Frigo and S. Johnson, FFTW Manual, http://www.fftw.org/.

Hindawi

Submit your manuscripts at
http://www.hindawi.com